Progress In Electromagnetics Research, Vol. 162, 1–14, 2018

Microwave Non-invasive Temperature Monitoring Using UWB Radar for Cancer Treatment by Hyperthermia

Ondrej Fiser[1, *], Marko Helbig[2], Jürgen Sachs[3], Sebastian Ley[2], Ilja Merunka[4], and Jan Vrba[4]

Abstract—*Objective:* In this paper we present a study of a novel method to noninvasively monitor temperature during thermotherapy for instance in cancer treatment using M-sequence radar technology. The main objective is to investigate the temperature dependence of reflectivity in UWB radar signal in gelatine phantoms using electrically small antennas. *Methods:* The phantom was locally heated up, and consequently changes of signal reflectivity were observed. *Results:* An approximate linear relationship between temperature change and reflectivity variations was formulated. To show the potential of this approach we used an M-sequence MIMO radar system. The system was tested on breast-shape phantom with local heating by circulating water of controlled temperature. Delay and Sum algorithm was implemented for two-dimensional imaging. *Significance:* The article is a study of temperature measurement using UWB radar system for possible usage in thermotherapy.

1. INTRODUCTION

Thermotherapy is a medical treatment aimed to trigger many therapeutic effects of heat on patient's body. Thermotherapy can be classified in accordance with the size of the heated area in local and regional treatment [1]. In both cases continuous temperature monitoring is important for patient safety and treatment effectiveness. Continuous temperature monitoring is needed to provide the thermal feedback in the treated and surrounding areas, within the correct therapeutic range. There are three thermotherapeutic approaches: diathermia (temperature increase of tissue by 1–3°C, particularly used in physiotherapy), hyperthermia (temperature increase by 4–8°C in treated tissue, mostly used in oncology) and ablation (temperature increase by 20–30°C, used in oncology, urology, cardiology etc.).

The most widely used method of continuous temperature measurement in thermotherapy is the implementation of invasive probes (optical catheters) in tumours [2]. This method is inexpensive and fast, but it provides information about the temperature from only a few points. For more comprehensive information about temperature distribution a high number of catheters are required. However, this procedure causes pain and general patient discomfort. A more suitable alternative is noninvasive temperature monitoring, using one of these techniques:

1) Magnetic resonance imaging (MRI).
2) Microwave radiometry.
3) Ultrasound based techniques.

Received 16 November 2017, Accepted 16 April 2018, Scheduled 2 May 2018
* Corresponding author: Ondrej Fiser (ondrej.fiser@fbmi.cvut.cz).
[1] Department of Biomedical Technology, Faculty of Biomedical Engineering, Czech Technical University in Prague, Czech Republic. [2] Institute of Biomedical Technology and Informatics, Faculty of Computer Science and Automation, Technische Universität Ilmenau, Germany. [3] Institute of Information Technology, Faculty of Electrical Engineering and Information Technology, Technische Universität Ilmenau, Germany. [4] Department of Electromagnetic Field, Faculty of Electrical Engineering, Czech Technical University in Prague, Czech Republic.

4) Microwave differential tomography.

An overview of possible methods for temperature monitoring for hepatic radiofrequency (RF) ablation brings article [3]. Frich defined ideal requirements for noninvasive thermometry during the ablation (temperature accuracy: < 1–$2°$C, spatial resolution: < 1–2 mm while low cost of the technology being a bonus). These requirements of noninvasive thermometry can also be assigned to the whole thermotherapy treatments.

The MRI temperature change detection method is based on measurement of temperature dependent MRI parameters (e.g., proton resonance shift, diffusion coefficient shift, spin-lattice relaxation time) [4]. Changes in these signals correlate with temperature change. Unfortunately, this method is very expensive. The microwave radiometry is based on the principle of the Planck's radiation law, for instance on measurement of power noise radiated from the measured tissue [5–7]. The third method is ultrasonic (US) temperature measurement based on change of US wave velocity in heated area and scattering variation of US wave [8]. Although cheaper than MRI, both radiometry and ultrasound based imaging are promising methods, but in early stages of development.

The microwave tomography is based on the reconstruction of the complex permittivity distribution. Then the reconstruction of the temperature profile is possible. The integration of the three-point steering system for the noninvasive temperature monitoring of high intensity focused ultrasound (HIFU) based on this method is described in [9, 10]. The system is composed of a monopole antenna circular array working on the frequency 0.9 and 1.1 GHz. Temperature resolution 0.2–0.5 °C (depending on type of the reconstruction algorithm) was achieved. In [11] the system validation of noninvasive temperature observation in small animal (small pigs) was performed. The other real-time microwave imaging system for thermal therapy based on the microwave differential tomography is described in [12] and is based on a similar principle.

The objective of this article is to study received ultra-wideband (UWB) radar signal behaviour in the case of the phantom heating and to extend our findings (presented in [13]) with more appropriate tests. Another objective of this work is to prove that this technology can be used in thermotherapy, specifically as a feedback for breast cancer hyperthermia. Our main research interest is the development of a new temperature monitoring system, based on UWB radar detection principle, for primary usage in hyperthermia. The methods based on the microwave radar were proposed by Miyakawa et al. [14, 15]. The tomographic method is used for the noninvasive detection of the temperature changes in the human body. The transmitting antenna emits radar chirp signal (1–2 GHz), and the signal is received on the opposite side of the human body. Conventional CT reconstruction algorithms are used for the evaluation and reconstruction of the temperature changes. The numerical method [16] for a reconstruction of the temperature profile in time-domain is described by Bolomey et al. The temperature profile is estimated through the reconstruction of the conductivity change in case the relative permittivity is equal to one.

The advantage of the UWB radar method for the thermometry against other methods is the assumption that the method is less numerically expensive, easy to implement and cost effective.

2. METHODS

2.1. UWB M-Sequence Radar

Our measurements were based on M-sequence radar technology developed at the Technische Universität Ilmenau. The energy of the pseudo-noise stimulus is distributed equally over time, while the stimulus signal is very time stable and robust, with low jitter and drift. This enables emission of relatively low signal magnitudes, and it makes the device suitable for medical purposes. The time response was computed through a cross-correlation between the stimulus signal and the measured signal from the medium under test (MUT). The M-sequence technology we used is further described in [17].

2.2. Detection Principle of Differential Temperature Measurement

The detection principle of temperature changes in the heated area using an UWB radar technology is based on measurement of backscattered signal differences due to the change of the contrasts in dielectric parameters incurred by temperature change.

Temperature dependent changes in tissue dielectric parameters were discussed, measured and modelled, e.g., in Lazebnik et al.'s study [18] using pork livers. As far as we know there are no other studies concerning our frequency band (1–6 GHz).

We derived equation of the relationship between phasor of received and transmitted signal intensity respecting continual reflection along the phantom. The temperature changes in time and volume as well as complex permittivity $\hat{\varepsilon}$ (and thus wave impedance $\hat{Z}$, where $\hat{}$ symbolizes complex number), see Fig. 1. Let's suppose that the signal is reflected by one borderline at distance x:

$$\hat{I}_R = \hat{I}_T \mathrm{e}^{-2\hat{\gamma}x} \hat{\Gamma}\,(x) \tag{1}$$

where $\hat{I}_R$ is the received signal intensity, $\hat{I}_T$ the transmitted signal intensity, x the distance from antennas to the point of reflection, $\hat{\Gamma}$ the reflection coefficient, and $\hat{\gamma}$ the propagation constant representing propagation speed and losses. The propagation constant $\hat{\gamma}$ is defined as:

$$\hat{\gamma} = 2\pi f \frac{\sqrt{\hat{\varepsilon}}}{c_0} \tag{2}$$

where c_0 is the speed of light in vacuum.

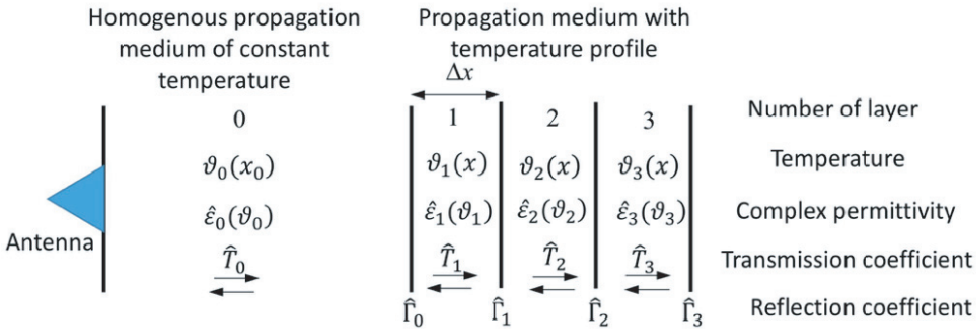

Figure 1. Layered model of locally heated medium under test (MUT).

If the temperature in the medium changes with distance x continuously, then the continuous borderlines reflect the signal rise. The "continuous" reflection can be formally expressed by the integration of Equation (1):

$$\hat{I}_R = \hat{I}_T \int_0^{\mathrm{L}} \mathrm{e}^{-2\int_0^x \hat{\gamma}_0(f)dx} \hat{\Gamma}\,(x)\,\mathrm{d}x \tag{3}$$

where L is the total length of the phantom. This equation is based on assumptions that the propagation constant $\hat{\gamma}$ is equal to $\hat{\gamma}_0$ from the attenuation point of view (not from the reflection coefficient viewpoint). The reflection coefficient is very small, and thus we can consider the unity transmission coefficient.

Reflection coefficient $\hat{\Gamma}$ of a layer boundary:

$$\hat{\Gamma}=\frac{\hat{Z}_{n+1}-\hat{Z}_n}{\hat{Z}_{n+1}+\hat{Z}_n} = \frac{\sqrt{\hat{\varepsilon}}_n - \sqrt{\hat{\varepsilon}}_{n+1}}{\sqrt{\hat{\varepsilon}}_n + \sqrt{\hat{\varepsilon}}_{n+1}} = \frac{\hat{\gamma}_n - \hat{\gamma}_{n+1}}{\hat{\gamma}_n + \hat{\gamma}_{n+1}} \approx -\frac{\Delta\hat{\gamma}_n}{2\hat{\gamma}_n} \tag{4}$$

considering $\Delta\hat{\gamma}_n = \hat{\gamma}_{n+1} - \hat{\gamma}_n$ and $|\Delta\hat{\gamma}_n| \ll 2\hat{\gamma}_n$. Substituting it to Equation (3) one can obtain:

$$\hat{I}_R=-\hat{I}_T \int_0^{\mathrm{L}} \mathrm{e}^{-2\int_0^x \hat{\gamma}_0(f)dx} \frac{\Delta\hat{\gamma}_n}{2\hat{\gamma}_n} dx \tag{5}$$

where $\hat{\gamma}_0$ is the propagation constant of medium at initial temperature, and f is the frequency. We assume a weak spatial variation of the propagation constant, and we can write $\hat{\gamma}_n \approx \hat{\gamma}_0$. For small $\Delta x -> 0$ it is valid:

$$\Delta\hat{\gamma}_n = \gamma' \Delta x \tag{6}$$

Derivation of the propagation constant γ' owing to distance x depends on temperature. And this temperature is dependent on distance x from antenna to the point of investigation. It can be expressed as:

$$\gamma'(x,f,\vartheta) = \frac{d\hat{\gamma}(f)}{d\vartheta}\frac{d\vartheta(x)}{dx} = \hat{\alpha}_\gamma(f)\vartheta'(x) \tag{7}$$

where $\hat{\alpha}_\gamma(f)$ is the temperature coefficient of the propagation constant, and $\vartheta'(x)$ represents the temperature gradient which we are interested in. Finally, we can obtain:

$$\hat{I}_R \approx -\hat{I}_T \frac{\hat{\alpha}(f)\,\Delta x}{2\hat{\gamma}_0(f)} \int_0^{\mathrm{L}} \mathrm{e}^{-2\int_0^x \hat{\gamma}_0(f)dx}\vartheta'(x)\,dx \tag{8}$$

From Eq. (8), we can observe that the reflection coefficient of the propagation medium at a given frequency depends on the temperature gradient. Hence, by the reflection coefficient over a large bandwidth measurement, an appropriate inversion of Eq. (8) may be used to reconstruct the temperature gradient $\vartheta'(x)$.

For the case of a radar measurement, the received signal in time domain follows from Eq. (7) as:

$$y(t) = h_r(t) * i_R(t) * h_t(t) * a(t) \tag{9}$$

Here, $*$ represents convolution; h_r andh_t are the impulse responses of the antennas in the receive and transmit mode; $a(t)$ is the stimulus signal; t is the propagation time. The impulse response of the propagation medium is assigned as $i_R(t)$, which is nothing but the inverse Fourier transform of Eq. (8). Note, however, that our simple plane wave model does not respect spherical wave propagation, and the permeability μ of the propagation medium is supposed to be constant.

In what follows, we are mainly interested in the observation of the temporal temperature variation due to heating. For that purpose, we start the measurement at temperature equilibrium leading to the receive signal $y_0(t)$ which is taken for reference. This signal is subtracted from the measurement during heating. Since antenna impulse responses and sounding signal do not depend on the temperature, their actual time shape is out of interest.

2.3. Phantom

For our experiments a natural gelatine (agar) phantom, which is the testing standard for the microwave hyperthermia applicators at frequencies of 434, 915 and 2450 MHz, was used. Parameters of gelatine phantom were measured and described in [19]. The advantage of this type of phantom is its chemical stability at temperatures exceeding 80°C. We measured the frequency dependence of complex permittivity of an agar phantom at 20°C using available probe "Dielectric Assessment Kit" (DAK-12) from the Speag company working in the frequency band 10 MHz–3 GHz (measured at the Faculty of Biomedical Engineering, CTU Prague, Czech Republic). We fitted the measured data into a two-pole Cole-Cole model according to the Cole-Cole expression (10) using the MATLAB nonlinear regression tool:

$$\varepsilon'(\omega) - \mathrm{j}\varepsilon''(\omega) = \varepsilon_\infty + \sum_{k=1}^{\mathrm{N}} \frac{\Delta\varepsilon_k}{1+(\mathrm{j}\omega\tau_k)^{(1-\alpha_k)}} + \frac{\sigma_i}{\mathrm{j}\omega\varepsilon_0} \tag{10}$$

where ε' is the real part of complex permittivity; ε'' is the imaginary part of complex permittivity; N is the order of the Cole-Cole model (in our case $N = 2$); ε_∞ is the permittivity at infinite frequency; $\Delta\varepsilon_k$ is the dispersion magnitude described as $\Delta\varepsilon_k = \varepsilon_s - \varepsilon_\infty$ (ε_s is static permittivity); τ_k is the relaxation time constant; α_k is the pole broadening parameter fixed permanently to 0.1; σ_i is the static ionic conductivity. The complex permittivity dependence on temperature was determined using the Ellison model of complex permittivity of pure water (gelatin phantom consists of 96% of water) [20]. We assume that the complex permittivity of agar and water is proportional to the temperature for both real (ε'_r) and imaginary (ε''_r) parts. The proportionality factor is also frequency dependent. To estimate the temperature dependence of dielectric parameters the following approximate Equations (11) and (12) were proposed:

$$\varepsilon'_r(\mathrm{agar},f,\vartheta) \approx \varepsilon'_r(\mathrm{agar},f,\vartheta_0)\cdot\frac{\varepsilon'_r(\mathrm{water},f,\vartheta)}{\varepsilon'_r(\mathrm{water},f,\vartheta_0)} \tag{11}$$

where ϑ_0 is the temperature at the time of measurement (20°C), and ϑ is the temperature for which we want to estimate the dielectric parameters. Similarly

$$\varepsilon_r''\left(\text{agar}, f, \vartheta\right) \approx \varepsilon_r''(\text{agar}, f, \vartheta_0) \cdot \frac{\varepsilon_r''(\text{water}, f, \vartheta)}{\varepsilon_r''(\text{water}, f, \vartheta_0)} \tag{12}$$

In Fig. 2 the estimated course of real part of relative permittivity (a) and the imaginary part of relative permittivity (b) depending on frequency and temperature in the 20–45°C range are shown. The blue curve is the modeled course from measurement while other curves are estimated by suggested temperature dependence (derived from Equations (11) and (12)). The relative permittivity change is approximately 2% per 5°C. Values of imaginary part of relative permittivity are changing approximately by 14% per 5°C (for temperature range 20–30°C). Our current investigations is focused on measuring the temperature dependent complex permittivity of liquids as well as solid materials. Therefore, we suggested an improved temperature dependent calibration approach which is described in [21].

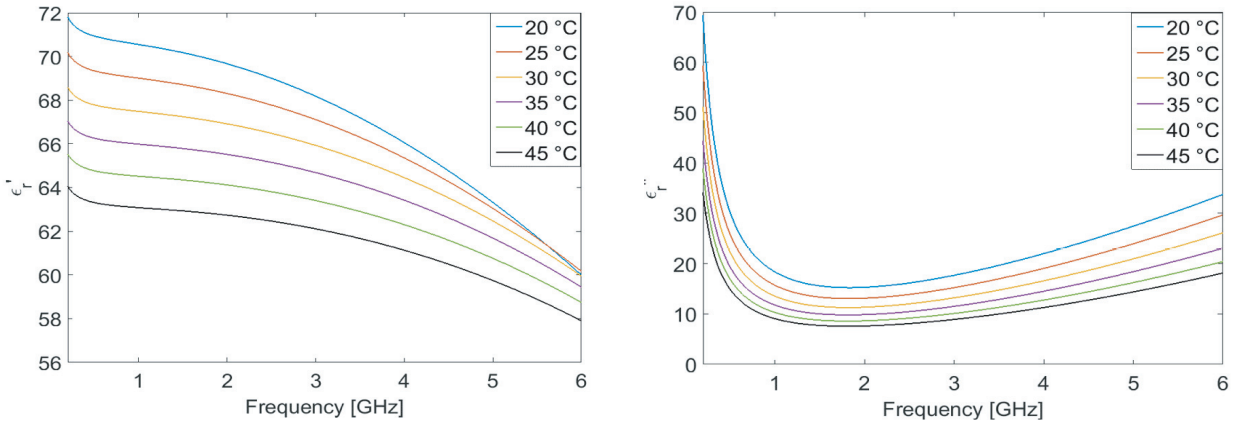

Figure 2. Estimation of temperature dependency of (a) real part relative permittivity and (b) imaginary part of relative permittivity of agar phantom using Equation (11) or (12).

2.4. Signal Processing

To analyse the received signals and to obtain the response caused by local temperature increase or decrease, we had to deal with specific strong effects affecting the signal of our interest. These interrupting effects must be carefully removed from the signals (without influencing the signal of interest). For these reasons, we performed the following steps: a) clutter extraction, b) drift and c) losses elimination. These procedures are further described in [13, 22]. For simplicity we did not anticipate the frequency-dependent tissue losses. Thus we created differential signal $y_d\left(t, \tau\right)$ (difference caused by heating effects) which is expressed from next equation:

$$y_d(t, \tau) = y_H\left(t, \tau\right) - \bar{y}_0(t) \tag{13}$$

where t is the propagation time; τ is the observation time; $y_d\ \left(t, \tau\right)$ is the signal difference caused by heating effects; $y_H(t, \tau)$ is the signal at a certain time of heating; $\bar{y}_0(t)$ is the mean signal representing the deterministic signal components computed from gained signals before heating (template). In all our measurements, the mean signal value was determined when the phantom was stabilized at temperature of 20°C.

3. TEMPERATURE CHANGE DETECTION EXPERIMENTS

We directly attached two "electrically small" (13×4 mm) active differentially fed (realized by differential amplifier) dipole antennas (in quasi mono-static radar mode), fixed to the agar phantom in which the

heating tube was inserted. The contact between the antenna and the phantom is crucial for signal quality and stability. We evaluated the contact quality according to the shape and amplitude of crosstalk between the antennas to maintain the same conditions as possible for each experiment. The heating tube is made from polymethylpentene material (TPX). According to our experiences this material has better adhesion to the phantom than glass even in the case of higher temperatures of liquids inside the heating tube. It does not create air gaps. Measurement setup layout can be seen in Fig. 3. We changed the heating method which we used in our previous experiments [13] (resistor and heating pump). Static water application as a heater allows us to avoid some random effects (random noise) caused by peristaltic pump vibrations. We expected the same change in the complex permittivity of water and agar with temperature. The next advantage of this heating method is that it enables heating and subsequently cooling of the phantom in a relatively short time without external intervention.

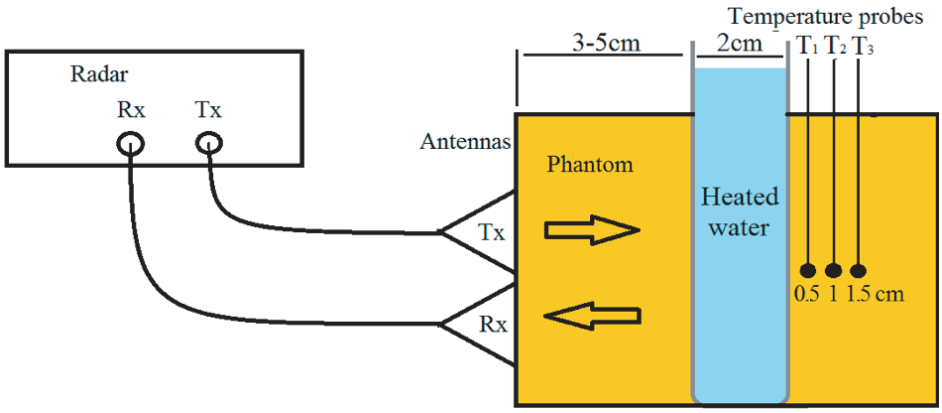

Figure 3. Measurement setup for initial experiment.

3.1. Experiment Process and Results

We prepared three phantoms with different distances (3–5 cm according to the Fig. 3) between antennas and heating tube. Into each phantom three temperature probes (PT 100) were placed at distances of 0.5, 1 and 1.5 cm from the heating tube.

In Table 1 there is an overview of temperature probes distances from antennas and heating tube. The probes were placed on the other side of heating tube (than antennas) to avoid unwanted responses from metal probes to electromagnetic wave. We assumed the same heating spreading in all directions from heating tube, and thus the measured temperature is totally correlated with the temperature on the other side of heating tube. We poured hot water into the tube (starting temperature was 87°C). Due to the thermal conductivity of the phantom, the heat was equally spreading to the surrounding area.

Table 1. Distances of temperature probes from antennas and heating tube.

T probe	$D_{antennas}$ [cm]	$D_{heating\ tube}$ [cm]
T_1	3.5	0.5
T_2	3	1
T_3	2.5	1.5

For these measurements we used an M-sequence radar system with one transmitting output (T_x) and two receiving inputs (R_x). Fig. 4(a) illustrates radar response in the case when the temperature was stable in all parts of the phantom (agar, testing-tubes and water). Fig. 4(b) shows the resulting radargram. The radargram is prepared respecting drift reduction, attenuation in phantom and clutter subtraction. Due to the knowledge of the dielectric properties of used phantom, we were able to calculate

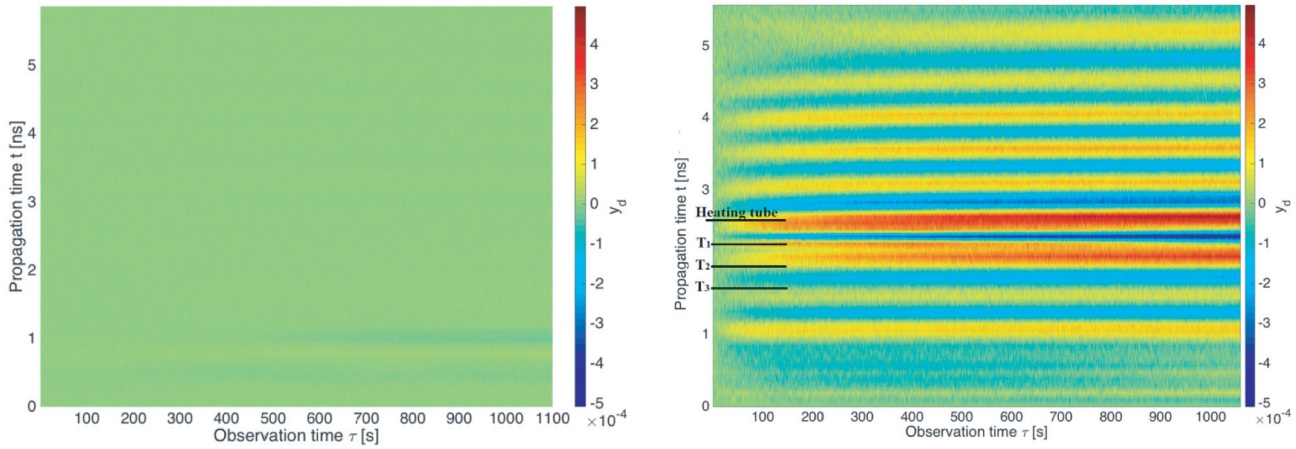

Figure 4. Radargrams for (a) temperature stabilized phantom and (b) heated phantom after clutter removal, drift and losses elimination (the heating tube was 4 cm from antennas). In (b) the estimated positions of heating tube and temperature sensors (T_1, T_2, T_3) are marked.

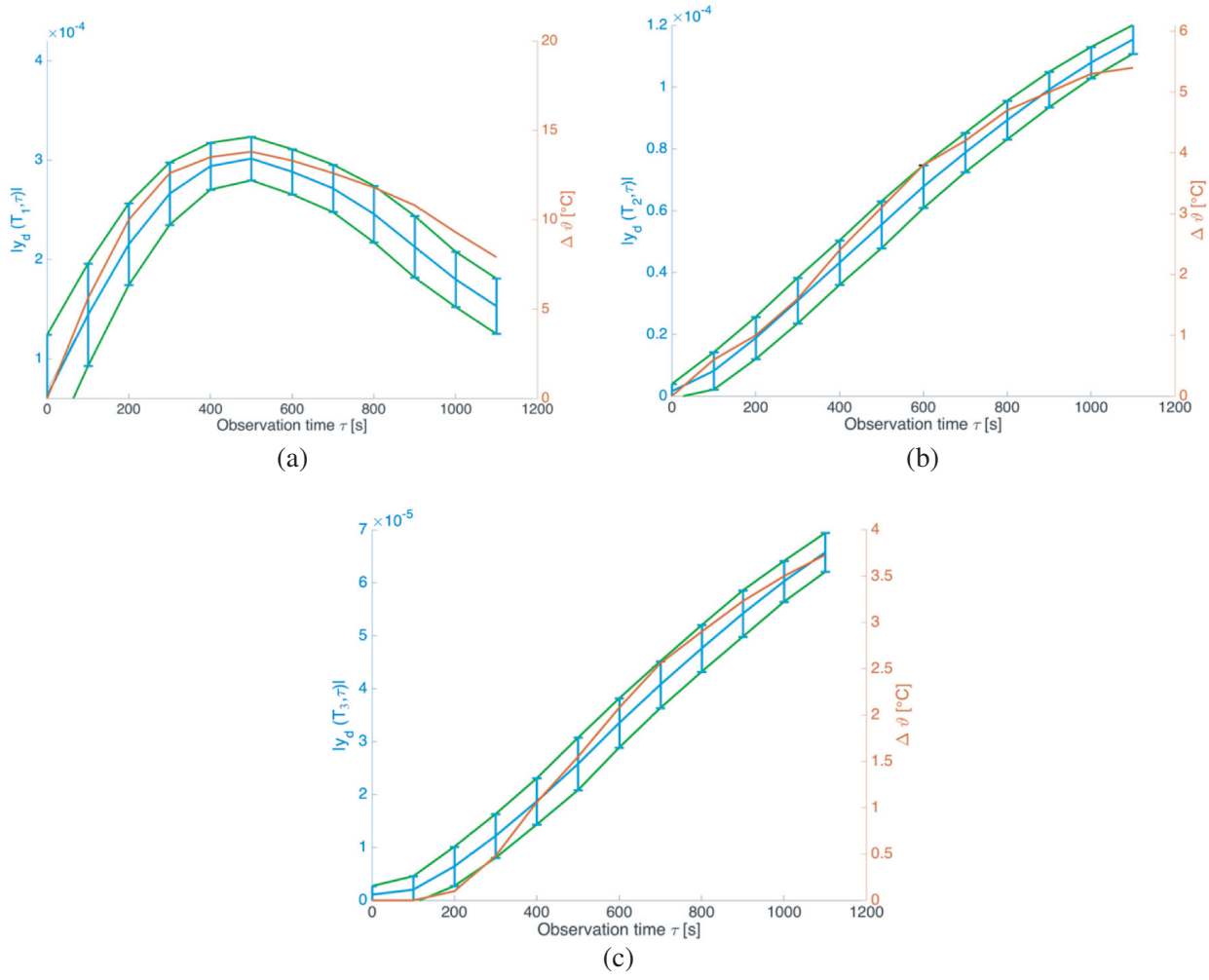

Figure 5. Radar response in position (a) T_1, (b) T_2 and (c) T_3.

the distance from the signal time line and thus find responses corresponding to the temperature probes positions. Results presented in this section are for the 4 cm distance between the heating tube and the antennas. This distance was chosen because it corresponds to the penetration depth of superficial hyperthermia to the muscle tissue for frequency 434 MHz.

Figure 5 displays absolute value of reflection variations in certain depth from the antennas in case of heating. We chose the positions according to the temperature probes' location. The blue curve represents the mean value of response ($|y_d|$) in time period 10 seconds. The green curves represent 95% confidence interval ($+/-2std$) of reflection variations. The red curve is the measured temperature at a given position gained from temperature probes (T_1, T_2 and T_3). The temperature curve and measured reflection change have nearly identical shapes. Fig. 6 represents the scatterplot of the reflection-temperature dependence for three different distances from antennas. One can see that the reflection is proportional to the temperature and this dependence can be approximated linearly very well while Pearson's correlation coefficient R is 0.992. From this approximation it is possible to estimate the temperature change from the reflection change.

From Figs. 6(a) and (b) we estimate linear change dependence of relative permittivity on increasing temperature. This approximation should be applied also for different temperature ranges. In the scatterplot in Fig. 6(b) the radar responses of three independent measurements are shown with a correlation factor being $R = 0.967$. The slope is specific for each material.

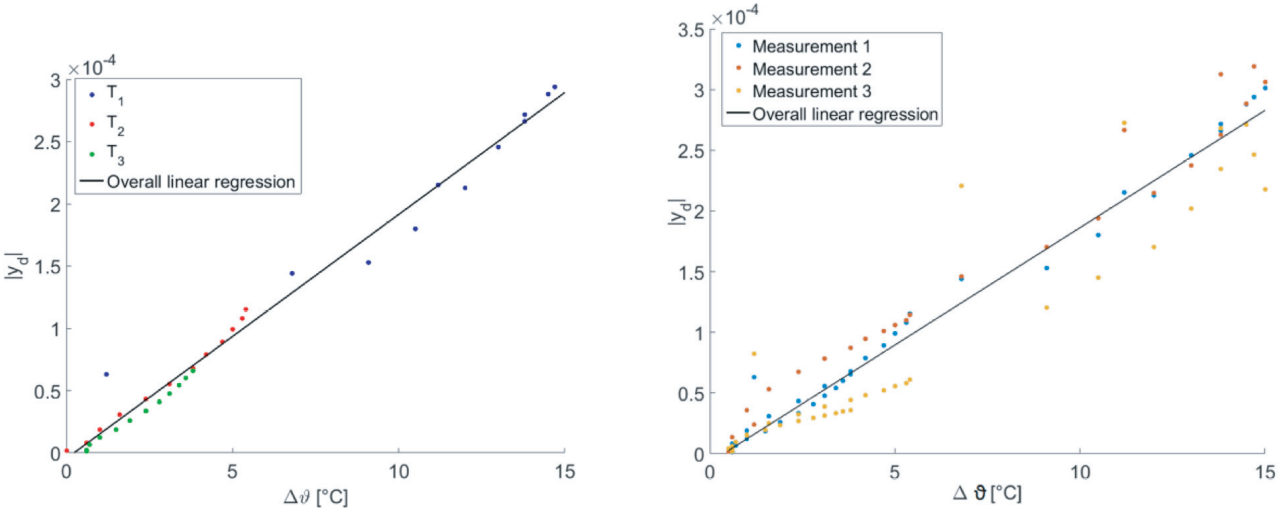

Figure 6. (a) The temperature change dependence of UWB radar reflectivity with linear regression curve of one measurement and (b) three independent measurements. Distance heating tube from antennas: Measurement 1 = 4 cm, Measurement 2 = 3 cm, Measurement 3 = 5 cm.

3.2. Estimation of Method Resolution

The temperature resolution of noninvasive differential thermal measurement is dependent on UWB signal bandwidth, signal to noise ratio (SNR), and attenuation in phantom. The resolution decreases with increasing distance from antennas. This is caused by a higher attenuation correction which leads to higher noise. The average temperature resolution of the applied method is determined according to the following estimation:

$$\Delta\vartheta_{res}(t,\tau) = \vartheta\left\{\bar{y_d}\left(t,\tau\right) + 2\cdot\, std\left(t,\tau\right)\right\} - \vartheta\left\{\bar{y_d}\left(t,\tau\right)\right\} \tag{14}$$

where $\Delta\vartheta_{res}\ (t,\tau)$ is the temperature resolution of the method, ϑ the temperature, $\bar{y_d}(t,\tau)$ the mean reflectivity in time interval t (more measurements performed), and $std(t,\tau)$ the standard deviation of this reflectivity ensemble in time t (level of significance 5%). The standard deviation is affected by Gaussian

noise of the whole system and by repeatability of the measurement. The resolution was estimated for all three positions separately, because the standard deviation was different. The dependence of temperature difference on intensity y_d used in Equation (13) can be expressed by regression formula (15).

$$|y_d(t,\tau)| = 1.9{\cdot}10^{-5}{\cdot}\Delta\vartheta - 0.7{\cdot}10^{-5} \tag{15}$$

where $\Delta\vartheta$ is the temperature difference. The offset in the formula (15) is caused by the dispersion and uncertainty of the measurement. Calculated method resolutions $\Delta\vartheta_{res}$ and measured standard deviations are listed in Table 2.

Table 2. Estimation of temperature resolution and standard deviation of used method.

Position	T_1	T_2	T_3
$\Delta\vartheta_{res}$ [°C]	1.3	0.77	0.41
$2\,std$ [-]	$1.17 \cdot 10^{-4}$	$6.55 \cdot 10^{-5}$	$3.45 \cdot 10^{-5}$

4. DIFFERENTIAL TEMPERATURE IMAGING USING MIMO SYSTEM

The goal of this experiment was to show the potential of temperature difference distribution in two or three dimensions. For this experiment we have used the UWB MIMO M-sequence radar connected to a hemispherical antenna array in a multi-static mode containing 24 active antennas arranged in a breast shape (see Fig. 7(a)). This experimental system was developed at the Technische Universität Ilmenau (Germany).

4.1. Breast Shape Phantom

For experiments using the MIMO system, we developed a curved breast phantom with the heating possibility (based on tissue mimicking oil-gelatin phantoms) according to [23]. The phantom was composed of 3 mm thick skin (made from silicon with carbon powder) and was filled by gelatin phantom material ($\varepsilon'_r = 68$ and $\sigma = 2\,\mathrm{S/m}$ for 3 GHz) [15]. Used phantom filling contained only gelatin. We used this phantom because of higher melting temperature than phantoms with higher oil content. In the center of the phantom a thin tube was placed. The tube was connected to the water pump of internal heating. During the experiment the continuously heated water was circulated through the phantom. Phantom with antenna array layout (a) and measurement setup are shown in Fig. 7.

4.2. 2D Image Reconstruction

For the image reconstruction of backscattered energy, the two-dimensional space-time beamformer algorithm "Delay and Sum" (DAS) was implemented. For each two-dimensional image reconstructions, signals from 16 antennas (8 transmitters and 8 receivers) were used. To improve the final image we left out channels (from reconstruction procedure) of an angle wider than 90° between antennas according to [24].

The DAS algorithm enables calculation of the sum intensity of each focal point respecting antenna positions and using knowledge of average propagation wave velocity in the phantom. The DAS algorithm can be described according to the following formula for multi-static antenna array [25]. The signal intensity I of focal point (r_0) is:

$$I(\mathbf{r}_0) = \left(\sum_{n=1}^{N} \sum_{\tau_w=-T_w/2}^{T_w/2} y_{d,n}(\tau_n(\mathbf{r}_0) + \tau_w) \right)^2 \tag{16}$$

where N is the number of channels, $y_{d,n}$ the recorded radar signal without clutter of channel n, $\tau_w(r_0)$ the time delay of focal point r_0, and τ_w the predefined time-window.

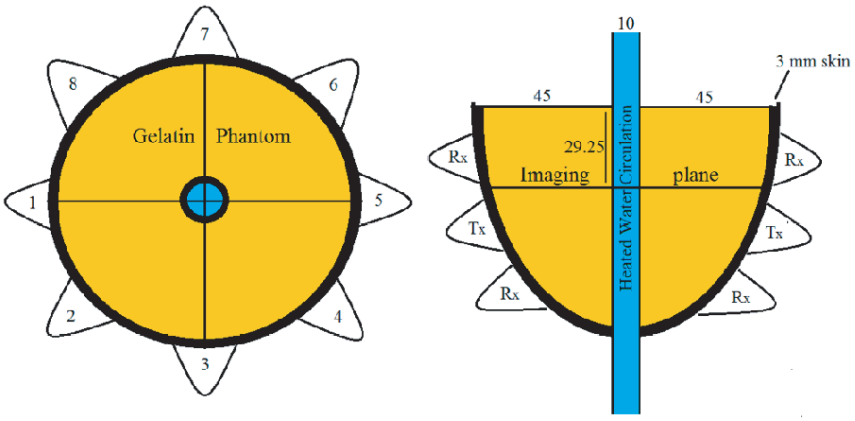

(a)

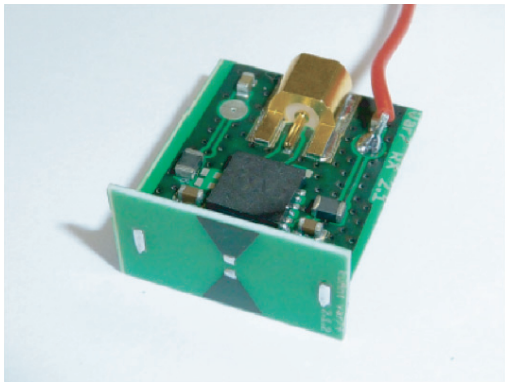

(b)

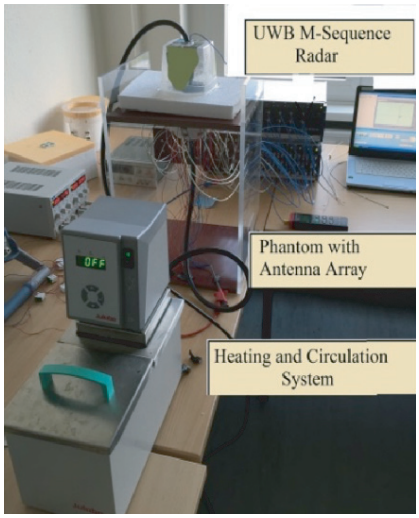

(c)

Figure 7. (a) Breast phantom with antennas placement, (b) active dipole antenna 8×4 mm used for imaging and MIMO measurement setup.

4.3. Experiment and 2D Imaging Results

Results from two-dimensional reconstruction using breast phantom are presented in Fig. 8. Initial state of all breast phantom parts was 20°C ($\tau = 0$ s). This is taken for the background subtraction. During the experiment the water inside the phantom was circulating and continuously heated from 20°C to 45°C, with steps being one degree per 7 seconds. The complete measurement duration was 480 seconds. The system is able to obtain all signals needed for reconstruction in every 8 seconds. Image reconstruction time needed for one image is around 20 seconds for all procedures involving signal processing. The reconstructed data are affected by artefacts which are obviously caused by insufficient number of antennas. With higher number of antennas, the inhomogeneity would decrease.

To correlate temperature change with intensity at given point we measured the temperature at two test points placed in the phantom (because of artefacts we choose points in the radiating axis of antenna where data are least affected by the artefacts). The first point was in fact the temperature of water circulating through the phantom (position [50 mm, 50 mm] in Fig. 8), and the second one was placed at a 2 cm distance from the center of the phantom (position [30 mm, 50 mm] in Fig. 8). Normalized data of intensity at focal points (which is a sum of all signals from given chosen distance r_0) coming from temperature measurement are demonstrated in Fig. 9. The normalized temperature is given by

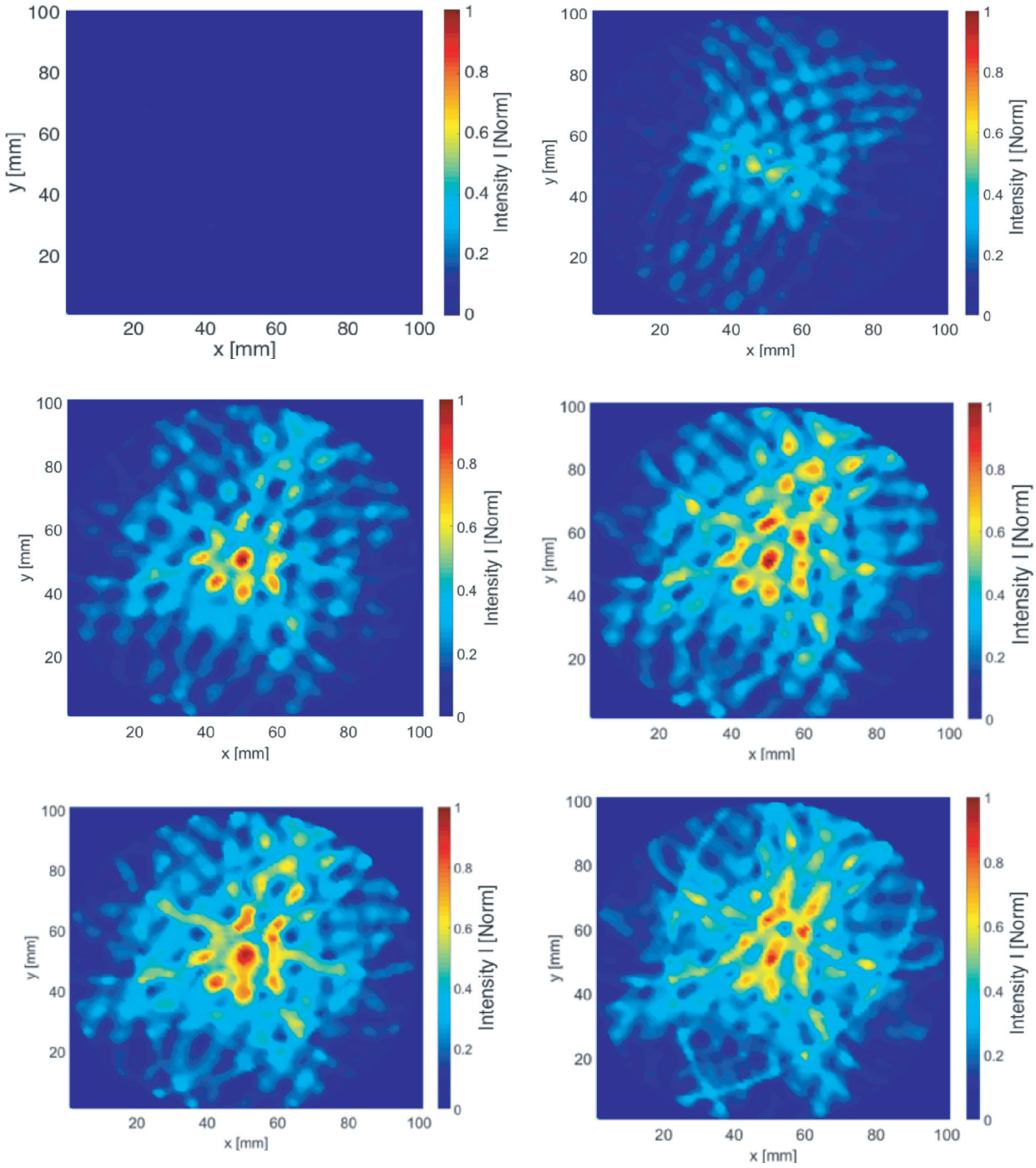

Figure 8. Reconstructed 2D results images obtained each 60 seconds.

the next relationship (17):

$$\vartheta_{norm} = \frac{\vartheta_{measured}}{\vartheta_{\max}} \tag{17}$$

The presented results of normalized rooted point intensity (sum of signals) of measured and normalized temperature (Fig. 9) are corresponding to our findings in previous section resulting in that the reflectivity is correlated with temperature (in nearly linear relation). The Pearson's correlation coefficient for water (blue curve) is $R = 0.97$. For gelatin phantom, orange curve is $R = 0.91$.

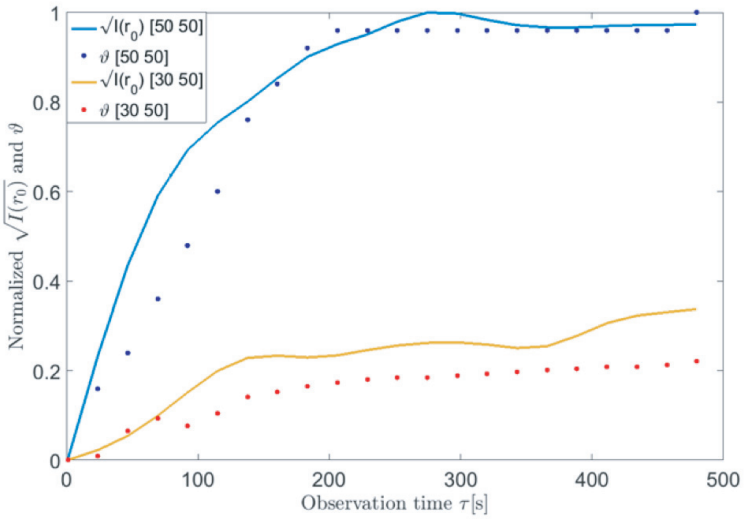

Figure 9. Normalized rooted point intensity $\sqrt{I(r_0)}$ of reconstructed 2D figures from Fig. 8 and corresponding temperature plotted in time dependence.

5. CONCLUSION

In this article we described the extension of our initial experiments with the reflected signal variations from a heated area. We further explained the temperature detection principle and proposed specific experiments with evaluation which were conducted to explore a correlation and relationship between changes in reflectivity and temperature. Results obtained from bi-static measurements were quantified. According to our results the UWB M-Sequence radar sensor technology is applicable to this kind of application. The experiment with homogenous phantom has shown that the sensor is able to detect weak signal variations at the depth of 3.5 cm with decent accuracy. The data from thermocouples were compared to the measured reflected signal intensity from the heated phantom. There was a good agreement. The result indicates that the spatial resolution of this method is sufficient. In our opinion, this method is feasible and stable with sufficient temperature and spatial resolution. It is suitable for clinical temperature monitoring usage in thermotherapy.

The second experiment concerned a breast shape phantom with an external heating system. For the measurement, an experimental MIMO system of 24 antennas was used. We implemented a two-dimensional reconstruction algorithm mainly based on generally known Delay and Sum algorithm. The system was tested on a proposed heterogeneous phantom of breast with heat applied. In this study we found that it is possible to detect changes in a UWB radar receiving signal caused by temperature changes within temperature ranges of hyperthermia treatment. The image refresh rate is now around 20 seconds, but this can be improved by faster hardware and better signal processing procedure implementation.

ACKNOWLEDGMENT

This work has been supported by a grant from the Czech Science Foundation, Number 17-20498J: “Non-invasive temperature estimation inside of human body based on physical aspects of ultra-wideband microwave channel” and the German Science Foundation (DFG) in the project HE 6015/2-1. Initially it was inspired by the COST Action TD1301: “Development of a European-based Collaborative Network to Accelerate Technological and Clinical in the Area of Medical Microwave Imaging”. In part it was supported by CTU grant SGS17/182/OHK3/3T/13 too.

REFERENCES

1. Vrba, J., M. Lapeš, and L. Oppl, "Technical aspects of microwave thermotherapy," *Bioelectrochemistry and Bioenergetics*, Vol. 48, No. 2, 305–309, May 1999.
2. Schena, E., D. Tosi, P. Saccomandi, E. Lewis, and T. Kim, "Fiber optic sensors for temperature monitoring during thermal treatments: An overview," *Sensors (Basel)*, Vol. 16, No. 7, Jul. 2016.
3. Frich, L., "Non-invasive thermometry for monitoring hepatic radiofrequency ablation," *Minim. Invasive Ther. Allied Technol.*, Vol. 15, No. 1, 18–25, Jan. 2006.
4. Wlodarczyk, W., M. Hentschel, P. Wust, R. Noeske, N. Hosten, H. Rinneberg, and R. Felix, "Comparison of four magnetic resonance methods for mapping small temperature changes," *Phys. Med. Biol.*, Vol. 44, No. 2, 607–624, Feb. 1999.
5. Klemetsen, Ø. and S. Jacobsen, "Improved radiometric performance attained by an elliptical microwave antenna with suction," *IEEE Transactions on Biomedical Engineering*, Vol. 59, No. 1, 263–271, Jan. 2012.
6. Dubois, L., J.-P. Sozanski, V. Tessier, J.-C. Camart, J.-J. Fabre, J. Pribetich, and M. Chive, "Temperature control and thermal dosimetry by microwave radiometry in hyperthermia," *IEEE Transactions on Microwave Theory and Techniques*, Vol. 44, No. 10, 1755–1761, Oct. 1996.
7. Karathanasis, K. T., I. A. Gouzouasis, I. S. Karanasiou, and N. K. Uzunoglu, "Experimental study of a hybrid microwave radiometry-hyperthermia apparatus with the use of an anatomical head phantom," *IEEE Transactions on Information Technology in Biomedicine*, Vol. 16, No. 2, 241–247, Mar. 2012.
8. Arthur, R. M., W. L. Straube, J. W. Trobaugh, and E. G. Moros, "Non-invasive estimation of hyperthermia temperatures with ultrasound," *International Journal of Hyperthermia*, Vol. 21, No. 6, 589–600, Sep. 2005.
9. Meaney, P. M., T. Zhou, M. W. Fanning, S. D. Geimer, and K. D. Paulsen, "Microwave thermal imaging of scanned focused ultrasound heating: Phantom results," *International Journal of Hyperthermia*, Vol. 24, No. 7, 523–536, Jan. 2008.
10. Meaney, P. M., K. D. Paulsen, M. W. Fanning, D. Li, and Q. Fang, "Image accuracy improvements in microwave tomographic thermometry: Phantom experience," *International Journal of Hyperthermia*, Vol. 19, No. 5, 534–550, Jan. 2003.
11. Meaney, P. M., et al., "Microwave thermal imaging: Initial in vivo experience with a single heating zone," *International Journal of Hyperthermia*, Vol. 19, No. 6, 617–641, 2003.
12. Haynes, M., J. Stang, and M. Moghaddam, "Real-time microwave imaging of differential temperature for thermal therapy monitoring," *IEEE Transactions on Biomedical Engineering*, Vol. 61, No. 6, 1787–1797, Jun. 2014.
13. Fiser, O., M. Helbig, S. Ley, J. Sachs, and J. Vrba, "Feasibility study of temperature change detection in phantom using M-sequence radar," *2016 10th European Conference on Antennas and Propagation (EuCAP)*, 1–4, 2016.
14. Miyakawa, M., "Tomographic measurement of temperature change in phantoms of the human body by chirp radar-type microwave computed tomography," *Med. Biol. Eng. Comput.*, Vol. 31 Suppl, No. S1, S31-6, Jul. 1993.
15. Bertero, M., M. Miyakawa, P. Boccacci, F. Conte, K. Orikasa, and M. Furutani, "Image restoration in chirp-pulse microwave CT (CP-MCT)," *IEEE Transactions on Biomedical Engineering*, Vol. 47, No. 5, 690–699, May 2000.
16. Bolomey, J.-C., C. Durix, and D. Lesselier, "Determination of conductivity profiles by time-domain reflectometry," *IEEE Trans. Antennas Propag.*, Vol. 27, No. 2, 244–248, Mar. 1979.
17. Sachs, J., *Handbook of Ultra-Wideband Short-Range Sensing: Theory, Sensors, Applications*, Wiley-VCH, Berlin, 2012.
18. Lazebnik, M., M. C. Converse, J. H. Booske, and S. C. Hagness, "Ultrawideband temperature-dependent dielectric properties of animal liver tissue in the microwave frequency range," *Phys. Med. Biol.*, Vol. 51, No. 7, 1941–1955, Apr. 2006.

19. Kato, H., M. Hiraoka, and T. Ishida, "An agar phantom for hyperthermia," *Medical Physics*, Vol. 13, No. 3, 396–398, May 1986.
20. Ellison, W. J., "Permittivity of pure water, at standard atmospheric pressure, ver the frequency range 0–25 THz and the temperature range 0–100°C," *Journal of Physical and Chemical Reference Data*, Vol. 36, No. 1, 1–18, 2007.
21. Ley, S., O. Fiser, I. Merunka, J. Vrba, J. Sachs, M. Helbig, "Preliminary investigations for reliable temperature dependent UWB dielectric spectroscopy of tissues and tissue mimicking phantom materials," Accepted to the *European Conference on Antennas and Propagation (EuCAP)* in London, Apr. 2018.
22. Helbig, M., J. Sachs, F. Tansi, and I. Hilger, "Experimental feasibility study of contrast agent enhanced UWB breast imaging by means of M-sequence sensor systems," *2014 8th European Conference on Antennas and Propagation (EuCAP)*, 311–315, 2014.
23. Lazebnik, M., E. L. Madsen, G. R. Frank, and S. C. Hagness, "Tissue-mimicking phantom materials for narrowband and ultrawideband microwave applications," *Phys. Med. Biol.*, Vol. 50, No. 18, 4245, 2005.
24. Helbig, M., M. Kmec, J. Sachs, C. Geyer, I. Hilger, and G. Rimkus, "Aspects of antenna array configuration for UWB breast imaging," *2012 6th European Conference on Antennas and Propagation (EUCAP)*, 1737–1741, 2012.
25. Conceição, R. C., J. J. Mohr, and M. O'Halloran, Eds., *An Introduction to Microwave Imaging for Breast Cancer Detection*, Springer International Publishing, Cham, 2016.